pubs.acs.org/Biomac

Article

Polymer Micelles vs Polymer–Lipid Hybrid Vesicles: A Comparison Using RAW 264.7 Cells

Carina Ade, Xiaomin Qian, Edit Brodszkij, Paula De Dios Andres, Järvi Spanjers, Isabella N. Westensee, and Brigitte Städler*

Cite This: *Biomacromolecules* 2022, 23, 1052–1064

Read Online

ACCESS | Metrics & More | Article Recommendations | Supporting Information

ABSTRACT: Bottom-up synthetic biology aims to integrate artificial moieties with living cells and tissues. Here, two types of structural scaffolds for artificial organelles were compared in terms of their ability to interact with macrophage-like murine RAW 264.7 cells. The amphiphilic block copolymer poly(cholesteryl methacrylate)-*block*-poly(2-carboxyethyl acrylate) was used to assemble micelles and polymer–lipid hybrid vesicles together with 1,2-dioleoyl-*sn*-glycero-3-phosphocholine or 1,2-dioleoyl-*sn*-glycero-3-phosphoethanolamine (DOPE) lipids in the latter case. In addition, the pH-sensitive fusogenic peptide GALA was conjugated to the carriers to improve their lysosomal escape ability. All assemblies had low short-term toxicity toward macrophage-like murine RAW 264.7 cells, and the cells internalized both the micelles and hybrid vesicles within 24 h. Assemblies containing DOPE lipids or GALA in their building blocks could escape the lysosomes. However, the intracellular retention of the building blocks was only a few hours in all the cases. Taken together, the provided comparison between two types of potential scaffolds for artificial organelles lays out the fundamental understanding required to advance soft material-based assemblies as intracellular nanoreactors.

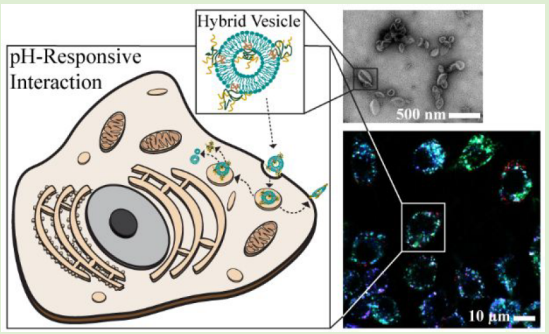

INTRODUCTION

Nanoparticle-based assemblies are an essential part of bottom-up synthetic biology that aims to integrate synthetic materials with cells and tissues.[1,2] Artificial organelles are an example in this context that are envisioned to equip mammalian cells with nanoreactors to substitute for missing function or even to impose non-native activity as discussed in several recent reviews.[3−5] The first reports in this context emerged over 12 years ago and were typically focused on producing fluorescent molecules in artificial organelles for facile detection, as summarized in an early review by Peters et al.[6] Recent efforts enriched the spectrum to more biologically relevant functions, such as the intracellular catalytic production of the biologically important molecule nitric oxide,[7] the intracytoplasmic capturing of doxorubicin in noncancerous cells,[8] and the intracellular production of cyclic guanosine monophosphate using encapsulated inducible nitric oxidase synthase and soluble guanylyl cyclase[9] as well as the scavenging of reactive oxygen species.[10−15] In addition to immortalized cell lines, artificial organelles were also explored in primary fibroblasts,[16] zebrafish,[17] rabbits,[18] and mice.[19,20]

Conceptually, artificial organelles consist of the active unit, typically enzymes, and a carrier that provides the compartment. For the latter, polymersomes are currently the preferred polymeric assemblies likely due to their vesicular nature, which allows for the encapsulation of enzymes, and their structural stability.[21,22] However, they often exhibit low inherent permeability that requires the incorporation of membrane channels or the use of external triggers to facilitate access of substrates to the encapsulated enzymes.[23] Micelles remain largely unexplored as artificial organelles probably because they do not allow for the association with protein cargoes. However, with the advent of small organic catalysts as enzyme mimics instead of using natural enzymes, this is likely to change. Micelles are easy to assemble in monodisperse populations with inherent small sizes in the range of sub-100 nm, making them ideal candidates as artificial organelles. We recently demonstrated that EUK, a catalase and superoxide dismutase mimic, associated with micelles could protect host cells from hydrogen peroxide induced pressure.[14] Liposomes are popular in nanoformulations as recently outlined by Crommelin et al.[24] but are not often considered for the assembly of nanoreactors likely due to their inherent low stability and low permeability that hinders efficient encapsulated catalysis. Lipid–polymer hybrid vesicles (HVs) are assemblies that have a membrane

Received: October 27, 2021
Revised: December 22, 2021
Published: January 12, 2022

https://doi.org/10.1021/acs.biomac.1c01403
Biomacromolecules 2022, 23, 1052–1064

consisting of both lipids and amphiphilic block copolymers as outlined in earlier reviews[25,26] or in sections of more recent reviews.[27,28] They offer an alternative to polymersomes and liposomes that benefits from modern polymer chemistry and the inherent self-assembly capability of phospholipids, resulting in stable vesicles with sufficient permeability to be used for encapsulated catalysis. Amphiphilic block copolymers that are used in this context include poly(dimethylsilane)-*block*-poly(ethylene oxide)[29−31] and poly(butadiene)-*block*-poly(ethylene oxide).[32,33] We have focused our efforts on block copolymer with a poly(cholesteryl methacrylate) as the hydrophobic part while varying the types of hydrophilic extensions. For instance, HVs prepared from 1,2-dioleoyl-*sn*-glycero-3-phosphocholine (DOPC) and an amphiphilic block copolymer with poly(2-(dimethylamino)ethyl methacrylate) as the hydrophilic block were able to induce lysosomal escape via the proton sponge effect.[34] On the other hand, when the pH-responsive monomer 2-carboxyethyl acrylate (CEA)[35] was copolymerized with methionine methacryloyloxyethylester as the hydrophilic extension of the block copolymer, the retention of the HVs in the lysosomes of the HepG2 cells was found.[36] In general, the intracellular fate, for example, lysosomal escape, of these different carriers remains largely underexplored, whereas some advances have been made by employing cell penetrating peptides, such as the positively charged TAT or the negatively charged GALA, for increased cellular uptake and lysosomal escape.[16,37,38] Admittedly, the ensured cytosolic placement is an important aspect, but intracellular retention and association with other organelles are additional characteristics that need to be considered. In the former case, we recently demonstrated that the two different building blocks in the HVs had different cellular retentions in the HepG2 cells.[36] In the latter case, Zelmer et al. recently explored polymersomes modified with nuclear localization sequences toward the delivery of encapsulated cargo to the nuclei as an example toward organelle targeting.[39]

Here, we explore the use of the amphiphilic block copolymer poly(cholesteryl methacrylate)-*block*-PCEA (P1) for micelle assembly or as the polymeric building block in the HVs followed by the biological evaluation of these moieties in macrophage-like murine RAW 264.7 cells (Scheme 1). Specifically, we (i) assemble micelles using P1 including their modification with the pH-sensitive amphiphilic peptide GALA, (ii) characterize the HV assembly using P1 and either DOPC or 1,2-dioleoyl-*sn*-glycero-3-phosphoethanolamine (DOPE) as the lipids, and (iii) evaluate the short-term toxicity, the uptake efficacy, and the lysosome escape ability of the HVs and the micelles in macrophage-like murine RAW 264.7 cells.

Scheme 1. (a) Chemical Structure of Poly(cholesteryl Methacrylate)-*block*-Poly(2-carboxyethyl Acrylate) (P1);[a] (b) Simplified Schematic of the Uptake and Interaction of a Representative Assembly with RAW 264.7 Macrophages Including the Intracellular Fate

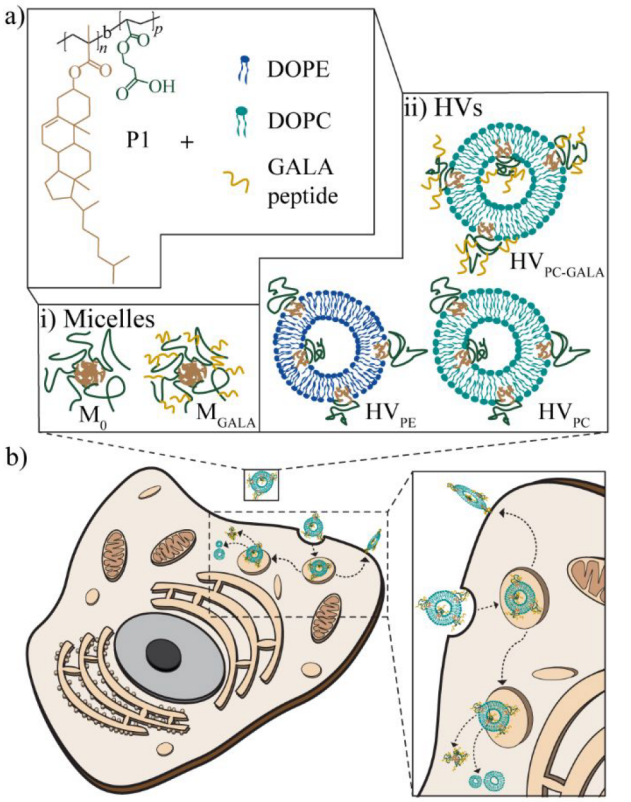

[a]Schematics of the used lipids 1,2-dioleoyl-*sn*-glycero-3-phosphocholine (DOPC) and 1,2-dioleoyl-*sn*-glycero-3-phosphoethanolamine (DOPE) and the GALA peptide and the assembled micelles (i, M_0 and M_{GALA}) and polymer−lipid hybrid vesicles (ii, HV_{PE}, HV_{PC}, and $HV_{PC\text{-}GALA}$) are also shown.

MATERIALS AND METHODS

Materials. 4-(2-Hydroxyethyl)piperazine-1-ethane-sulfonic acid (HEPES; 99.5%), 5(6)-carboxyfluorescein (CF), 6-dodecanoyl-*N*,*N*-dimethyl-2-naphthylamine (Laurdan), cell counting kit-8 (CCK-8), Dulbecco's Modified Eagle's Medium, hydrochloric acid (HCl), *N*-(3-(dimethylamino)propyl)-*N*′-ethylcarbodiimide hydrochloride (EDC), phosphate-buffered saline (PBS), pyrene, Triton-X-100 (TX), Sepharose CL-2B, sodium pyruvate, sodium bicarbonate, sodium acetate, sodium chloride (NaCl), sodium hydroxide (NaOH), and sucrose were purchased from Sigma-Aldrich. Dialysis tubing with a molecular weight cutoff (MWCO) of 3.5 kDa (Spectra/por 3), dimethyl sulfoxide (DMSO), membrane filters Nuclepore track etched (0.4 and 0.1 μm; Whatman), *N*-hydroxysuccinimide (NHS), poly(ether sulfone) membrane filters (0.45 μm), and tetrahydrofuran (THF) were purchased from VWR Chemicals. CellMask Deep Red plasma membrane stain and Oregon Green 488 Cadaverine 5-isomer (OG) were obtained from Thermo Fisher Scientific. Fetal bovine serum (FBS), LysoTracker Red DND-99, and LysoTracker Deep Red were purchased from Invitrogen, and penicillin−streptomycin (10 000 U/mL) was purchased from Gibco. 1,2-Dioleoyl-*sn*-glycero-3-phosphocholine (DOPC), 1,2-dioleoyl-*sn*-glycero-3-phosphoethanolamine (DOPE), 1,2-dimyristoyl-*sn*-glycero-3-phosphoethanol-amine-*N*-(lissamine rhodamine B sulfonyl) (^{Rho}PE), and cholesterol (Chol) were purchased from Avanti Polar Lipids. GALA peptide (WEAALAEALAEALAEHLAEALAEALEALAA) was obtained from GenScript.

HEPES buffer consisted of 10 mM HEPES and 150 mM NaCl at pH 7.4. Ultrapure water (18.2 MΩ cm resistivity) was provided by an ELGA Purelab Ultra system (ELGA LabWater, Lane End).

Poly(cholesteryl methacrylate)-*block*-poly(2-carboxyethyl acrylate) (P1) and the Oregon Green-labeled ^{f}P1 were synthesized as previously described. The poly(cholesteryl methacrylate) block and the poly(2-carboxyethyl acrylate) block had a molecular weight of 5 and 20 kDa, respectively.[40]

Micelle Assembly. P1 (4 mg) was dissolved in 40 μL of THF and added to 2 mL of HEPES buffer while stirring vigorously. The suspension was placed in an ice bath and subjected to a tip sonicator to sonicate for 40 min (10 s on, 5 s off, 10% amplitude). The obtained clear solution was centrifuged for 10 min (13.4×10^3 rpm) to remove impurities, and the supernatant was filtered through a syringe filter with a 0.45 μm poly(ether sulfone) membrane to remove large

https://doi.org/10.1021/acs.biomac.1c01403
Biomacromolecules 2022, 23, 1052−1064

aggregates. The solution was then transferred to a dialysis tubing (MWCO 3.5 kDa) and dialyzed against PBS buffer for 3 days with the buffer changed twice a day, resulting in M_0. Fluorescently labeled micelles ($^fM_0$) were assembled the same way by using the Oregon Green-labeled ^{f}P1 instead. The conjugation of the peptide GALA was performed by dissolving EDC (9.6 mg, 0.05 mmol) and NHS (2.9 mg, 0.025 mmol) in 100 μL of PBS followed by a dropwise addition to the M_0 or $^fM_0$ solution (~2 mL). The solution was slightly shaken and left to react for 15 min at room temperature. Afterward, GALA peptide (3 mg) in 200 μL of PBS was added dropwise, and the reaction was continued overnight at room temperature without stirring. The mixture was transferred to a dialysis tubing and dialyzed against PBS buffer for 3 days with the buffer changed twice a day, resulting in M_{GALA} or $^fM_{GALA}$. The micelle solutions were collected and stored in the fridge (4 °C) before use.

^{1}H NMR was used to confirm the GALA conjugation. To this end, M_{GALA} was dialyzed against ultrapure water to remove the salt and the sample was freeze-dried before dissolution in deuterated DMSO. ^{1}H NMR spectra were taken by a Bruker Ascend 400. The MestReNova software was used to analyze the spectra.

Micelle Characterization. Transmission electron microscopy (TEM) images were recorded on a Tecnai G2 spirit using 300 mesh copper Formvar/carbon grids (Ted Pella). The grids were made hydrophilic using glow discharge (45 s, air 10−15 mA), and 5 μL of sample was allowed to absorb on the grid (1 min) before excess liquid was blotted off. Negative staining was done twice with 3 μL of uranyl formate. The diameter of at least 120 micelles was measured in ImageJ to obtain size distributions. A Gauss curve was fitted to obtain the histogram, where the results are presented as mean ± std. dev. × 2 for 95.4% of the population.

Nanoparticle tracking analysis (NTA; Nanosight LM-10 instrument) was used to determine the hydrodynamic diameter (D_h) and particle concentration of the micelles. The micelle solutions were diluted (up to 200×) in PBS buffer before the measurements. Four measurements were conducted of each sample by taking a 1 min (1500 frame) static video with a camera level of 11−14. The measurement chamber was flushed with double distilled water and parts of the sample before advancing the sample manually from a 1 mL syringe. Additionally, the respective temperature was entered for each measurement ranging from 21.6 to 22.0 °C. NanoSight NT 3.1 software was used to analyze the videos using a detection threshold of 2−7 and auto blur size. Alternatively, D_h and the polydispersity index (PDI) of the micelles were determined by dynamic light scattering (DLS; Malvern Zeta sizer Nano-590 at a λ of 632 nm at 25 °C). The correlograms at pH 4 and 7.4 were recorded by diluting the sample 1:1 with HEPES buffer and adding 5 μL of HCl (1 M) to reach pH 4 and 5 μL of NaOH (1 M) to neutralize the pH to 7.4 again. Three measurements of three independent repeats were conducted.

The critical micelle concentration (CMC) of M_0 was determined by dissolving pyrene in a THF/HEPES solution (1:3, v/v) to prepare a 200 μM stock solution. Ten μL of the stock solution was added to 90 μL of micelle solutions with concentrations ranging from 0 to 2 mg mL^{-1}. The fluorescent intensities at λ_{em} = 374 nm (I_1) and λ_{em} = 383 nm (I_3) were subsequently measured with λ_{ex} = 337 nm. The I_1/I_3 coefficients were plotted against the concentrations of the micelles followed by linear fitting of the two parts of the graph to generate an inflection point. The corresponding concentration at the inflection point was determined as the CMC. Three independent repeats were conducted.

Hybrid Vesicle Assembly and Characterization. Hybrid vesicle (HV) assembly was performed using the film rehydration method. 0.4 mg of P1 or ^{f}P1 (5 mg mL^{-1} in THF) and 1.1 mg of lipids were combined (keeping a total mass of 1.5 mg). Either DOPC or DOPE (25 or 10 mg mL^{-1} in chloroform) was used, and 0.037 mg ^{Rho}PE (1 mg mL^{-1} in chloroform) was added, if applicable. The polymer and lipids were mixed in a 25 mL round-bottom flask and dried using constant rotation and a steady stream of nitrogen before attaching the flask to the vacuum line overnight for further drying. The rehydration step was performed by adding 1 mL of HEPES buffer and heating the flask to 37 °C in a water bath for 30 min for detachment followed by vortexing. The pH for rehydrating DOPE containing HV_{PE} was adjusted to 9 to ensure that a vesicular nature was favored. The solutions were extruded through a 400 nm membrane (21×) first and then a 100 nm membrane (21×) at room temperature. The extruded solutions were purified by size exclusion chromatography (SEC; Sepharose CL-2B) to separate the HVs from micelles and other small components. The resulting solutions of the HV or double-labeled ^{f}HV were collected and stored in the fridge (4 °C) before use. Additionally, liposomes were assembled as controls using 1.364 mg of DOPC and 0.099 mg of cholesterol (1 mg mL^{-1} in chloroform), and 0.037 mg of ^{Rho}PE was added before drying the film, resulting in $^{Rho}L_{PC}$.

Emission spectra analysis of the ^{f}HV was performed by adding 50 μL of the HV solution to a black 96-well plate, and the emission spectra of three independent batches of each sample were recorded at λ_{em} = 503−650 nm using λ_{ex} = 488 nm.

GALA Functionalization. It was not possible to directly conjugate GALA to the preformed HV_{PC}. Therefore, we first assembled M_{GALA} and recovered the polymer the same way as for the ^{1}H NMR measurements to use this polymer ($P1_{GALA}$) for the HV formation. Specifically, 1.1 mg of DOPC lipid (and 0.037 mg of ^{Rho}PE (1 mg mL^{-1} in chloroform) if required) was added in a round-bottom flask and dried using a rotary evaporator (Heidolph G5) for 10 min followed by further drying on the vacuum line overnight. One mL of HEPES buffer was used for rehydration followed by 5 min of vortexing to support detachment. Then, 0.4 mg of $^fP1_{GALA}$ dissolved in DMSO (5 mg mL^{-1}) was introduced, and the mixture was dialyzed (3500 MWCO) for 2 days against HEPES buffer at room temperature, replacing the HEPES buffer daily to remove DMSO while $P1_{GALA}$ was incorporated with the DOPC lipids. The solution was then extruded and purified by using SEC as outlined above, resulting in $HV_{PC\text{-}GALA}$ or $^fHV_{PC\text{-}GALA}$.

Vesicle Membrane Permeability. The carboxyfluorescein (CF) quenching assay was used to validate the alternative HV formation approach and to compare to pristine DOPC liposomes. To this end, CF (25 mM final CF concentration) was added to the samples between the dialysis and extrusion step. It should be noted that the pH had to be raised to 12 to ensure the complete dissolution of CF. The following purification by SEC was conducted in HEPES buffer at pH 7.4 to change the pH of the eluted fractions to pH 7.4. CF leakage measures of $HV_{PC\text{-}GALA}$ were performed at room temperature and compared to pristine DOPC liposomes. 100 μL sample was added to a black 96-well plate, and the CF emission was measured before and after TX (1% final concentration) addition every 24 h for 5 days. The data was normalized to the maximum release after disrupting the vesicles with TX on day 0.

pH Sensitivity. D_h, PDI, and the concentration of the micelles/vesicles were determined using DLS and NTA as described above. D_h and PDI of HV_{PE} upon a stepwise decrease of the pH were obtained from DLS measurements by adding HCl (0.1 or 0.01 M) to reach pH values between 7.4 and 4. The correlograms upon pH cycling and TEM images were obtained as described above. In the former case, only 4.5 μL of HCl and NaOH were added, and in the latter case, at least 120 vesicles were measured in ImageJ to obtain the size distributions. A Gauss curve was fitted to obtain the histogram, where the results are presented as mean ± std. dev. × 2 for 95.4% of the population.

Membrane Packing. The HVs' general polarization (GP) values were determined as an indication of membrane packing. To this end, the fluorescent membrane probe Laurdan was employed. 50 μL of sample, 50 μL of HEPES buffer, and 1 μL of Laurdan (0.25 mg mL^{-1} in DMSO) were added to a well in a black well plate and incubated under mild shaking for 45 min. Fluorescent spectra were recorded on a multiplate reader (PerkinElmer Ensight) at a λ_{ex} of 340 nm, and the emission spectra were recorded between a λ_{em} of 400 and 600 nm. The Laurdan spectra were normalized to the intensity peak at 490 nm. The GP was calculated following the equation below with the intensity at 440 nm (I_{440}) and 490 nm (I_{490}) being the blue- and red-shifted peak of the spectra, respectively. Three independent repeats were conducted.

https://doi.org/10.1021/acs.biomac.1c01403
Biomacromolecules 2022, 23, 1052−1064

$$GP = \frac{I_{440} - I_{490}}{I_{440} + I_{490}}$$

Giant Unilamellar Vesicle (GUV). GUVs were assembled by electroformation. Ten μL of DOPC (25 mg mL^{-1}) and 1 μL of ^{Rho}PE (1 mg mL^{-1}), if required, were mixed in a vial, and the mixture was evenly spread to a thin layer on an indium tin oxide (ITO)-coated glass coverslip (VesiclePrepChamber, Nanion Technologies GmbH, München). The film was dried overnight in a vacuum chamber. A 18 × 1 mm O-ring was placed on this coverslip, and another ITO-coated coverslip was placed on top. The space between the coverslips was filled with 290 μL of buffer solution (300 mM sucrose and 1 mM HEPES, pH ~ 6.5) to rehydrate the lipid film. An AC electric field (5 V, 10 Hz) was applied for 2 h at 26 °C to generate the GUVs or ^{Rho}GUVs. The GUVs were transferred to a vial and stored at 4 °C before imaging.

Visualization of GUV: Micelle/Vesicle Interaction. In order to image the interaction of micelles or vesicles with GUVs, 2−5 μL of GUV solution was added into a drop of 25 μL of HEPES buffer placed on a glass coverslip. Then, 5−18 μL of micelle ($^{f}M_0$ or $^{f}M_{GALA}$) or vesicle ($^{f}HV_{PE}$, $^{f}HV_{PC}$, $^{f}HV_{PC\text{-}GALA}$, or $^{Rho}L_{PC}$) solution was added to the drop. Confocal laser scanning microscopy (CLSM; Carl Zeiss, Germany) images of three to five different areas were recorded. Then, the pH was lowered to 4−5 by the addition of 25−40 μL of sodium acetate buffer (40 mM, 150 mM NaCl), and at least three different areas were imaged. One to two μL of NaOH (0.5 M) was added to increase the pH, and again, at least three different images were recorded. At least two different batches of each sample were investigated this way. The gain of the images has been artificially enhanced afterward in the image analysis for better visualization without any influence on the shown line scans.

Cell Work. Macrophage-like murine RAW 264.7 cells were obtained from the European Collection of Authenticated Cell Cultures and cultured at 37 °C and 5% CO_2 in 25 cm^2 culture flasks in Dulbecco's Modified Eagle's Medium with 4500 mg L^{-1} glucose, sodium pyruvate, and sodium bicarbonate (passage window of the cells: 12−25). The medium was supplemented with 10% FBS and 1% streptomycin/penicillin.

Cell Viability. 40 000 RAW 264.7 cells were seeded per well in 96-well plates and incubated at 37 °C and 5% CO_2 overnight. A range of concentrations of micelles or vesicles diluted in media (including FBS) was added to the wells with a maximum concentration of 10 vol % in 100 μL of media, and the samples were incubated for 24 h at 37 °C and 5% CO_2. It should be noted that the HV_{PC}'s were previously shown to be stable for at least 48 h in media.[40] The concentration of the stock solutions of the micelles and vesicles was adjusted according to the concentration obtained from the NTA measurements to ensure exposure of the cells to similar amounts of particles. Three different types of viability assays were performed. First, the wells were washed twice with PBS buffer, and 100 μL of media containing 10 vol % CCK-8 was added to each well; then, the samples were incubated for 2 h at 37 °C and 5% CO_2 before the absorbance at the λ of 450 nm was read in a multimode plate reader (PerkinElmer EnSight). Second, the media was removed, and 100 μL of fresh media and 10 μL of MTT reagent were added, followed by an incubation for 4 h at 37 °C and 5% CO_2. Then, 100 μL of formazan solubilization solution was added, and the well plates were incubated for 18 h at 37 °C and 5% CO_2. The absorbance at λ = 570 nm was measured using a multimode plate reader, and the background consisting of only media treated with the reagents was subtracted from all the measurements. Third, a LDH cytotoxicity assay was performed by removing 50 μL of media from the wells and adding 50 μL of reagent mixture to each well followed by incubation at room temperature for 10 min. Then, 50 μL of stop solution was added, and the fluorescent intensity ($\lambda_{ex/em}$ = 560/590 nm) was measured using a multimode plate reader. The background fluorescence of only media was subtracted from all the measurements. The cell death was calculated using

$$\text{cell death \%} = \frac{\text{compound treated LDH} - \text{spontaneous LDH}}{\text{maximum LDH} - \text{spontaneous LDH}} \times 100$$

where *spontaneous* LDH corresponds to the signal of nontreated cells and *maximum* LDH corresponds to the signal of lysed cells. The cells were lysed by the addition of 10 μL of 10× lysis buffer and incubation at 37 °C and 5% CO_2 for 45 min, followed by the addition of reagent mix and stop solution. At least three independent repeats for each sample were conducted.

Uptake Experiments. RAW 264.7 cells were seeded in a 96-well plate (50 000 cells per well) and allowed to adhere overnight at 37 °C in 5% CO_2. The fluorescently labeled micelles and vesicles (12×10^8 mL^{-1} and 10×10^9 mL^{-1}, respectively) in 100 μL of media were added to each well and incubated at 37 °C in 5% CO_2 for 3, 6, or 24 h or for 6 h followed by 18 h of incubation in pristine cell media. Cells without any treatment were used as a reference. Then, each well was washed twice with PBS buffer, and the cells were scraped off the plate and suspended in 100 μL of PBS. The cell mean fluorescence (CMF) was recorded by flow cytometry (Guava easyCyte Single Sample Flow Cytometer, Merck) using a λ_{ex} of 488 nm. Between 1200 and 2000 cells were analyzed in triplicate for each sample, and three independent repeats were conducted. The autofluorescence of untreated cells was subtracted from all values, and the CMF was normalized to the fluorescence intensity of the respective concentrations of the micelles or vesicles, measured by the plate reader, to account for variations between the batches of micelles or vesicles. The statistical significance employed to compare the means was determined using a one-way analysis of variance (one-way ANOVA) followed by a Tukey's multiple comparison post hoc test.

The exocytosis of $^{f}M_0$ was assessed by measuring the fluorescent intensity of the media. To this end, RAW 264.7 cells were seeded and incubated overnight as outlined above, followed by incubation with 90×10^8 or 179×10^8 $^{f}M_0$ mL^{-1} for 6 h and resting in $^{f}M_0$-free, phenol-red free media for an additional 18 h. Then, 100 μL of media was transferred to a black 96-well plate, and the fluorescent intensity was measured by using the plate reader ($\lambda_{ex/em}$ = 488/526 nm). For comparison, 90×10^8 or 179×10^8 $^{f}M_0$ mL^{-1} was diluted in 100 μL of phenol-red free media, and the fluorescent intensity was measured ($\lambda_{ex/em}$ = 488/526 nm). This latter fluorescent intensity was considered the maximum attainable value. Three independent repeats were performed using the same batch of $^{f}M_0$.

Lysosomal Escape. RAW 264.7 cells (300 000 cells in 1 mL cell media) were seeded in a cell culture imaging dish (μ-Dish 35 mm, ibidi; or 35 mm confocal dish, VWR) and allowed to adhere overnight at 37 °C and 5% CO_2. Then, the cells were incubated with the fluorescently labeled micelles (12×10^8 mL^{-1}) for 6 h before being washed twice with PBS buffer and left in fresh media overnight. The fluorescently labeled vesicles, on the other hand, were left to incubate with the cells for 24 h before washing twice with PBS buffer. LysoTracker Red DND-99 in the case of the micelles or LysoTracker Deep Red in the case of the vesicles was diluted in prewarmed media to a final concentration of 50 nM. The area containing the cells was covered with 120 μL of the lysotracker-containing media, followed by 45 min of incubation at 37 °C and 5% CO_2. The cells were washed twice with PBS and in the case of the samples with micelle exposure incubated with CellMask Deep Red Plasma membrane stain (5 μg mL^{-1} in 120 μL of cell media) for 5 min. The cells were washed twice with PBS, and 170 μL of PBS was added for storage. The cells were visualized using a Zeiss LSM700 confocal laser scanning microscope. Five images at random locations with the same settings were taken per sample, and three independent experiments were performed. The gain of the images has been artificially enhanced afterward for better visualization without any influence on the colocalization calculations. The colocalization of the micelles or vesicles with the lysosomes was determined via the Manders' colocalization coefficient (MCC) using the Coloc 2 plug-in for ImageJ. Subtraction of the background (50 pixel ball pen size) and adjustment of the lower threshold level to 35 were performed before the analysis for all of the images.

RESULTS AND DISCUSSION

Micelle Assembly. The amphiphilic block copolymer P1 chosen here consisted of a 5 kDa poly(cholesteryl

https://doi.org/10.1021/acs.biomac.1c01403
Biomacromolecules 2022, 23, 1052−1064

methacrylate) (PCMA) as the hydrophobic block and a 20 kDa poly(2-carboxyethyl acrylate) (PCEA) as the hydrophilic extension.[40] The latter block is a pH-responsive polyanion with a hydrophilic-to-hydrophobic phase transition at pH 4.[35] In agreement with our previous results,[40] the self-assembly of P1 at pH 7.4 resulted in monodisperse micelles M_0 with an average diameter of the long axis of 21 ± 5 nm (Figure 1a), a

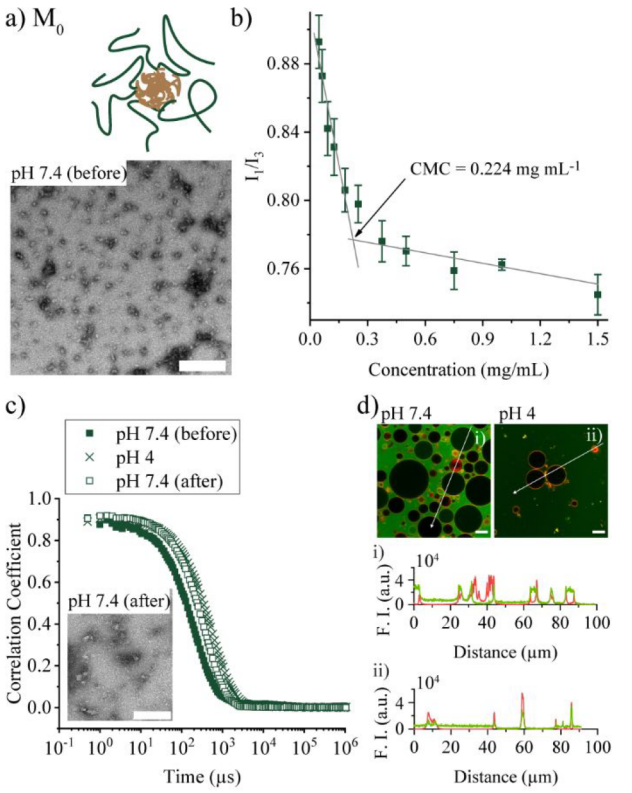

Figure 1. Micelle (M_0). (a) Cartoon representing M_0 and a representative TEM image of M_0 (scale bar 200 nm). (b) Determination of the CMC of M_0. (c) Correlograms obtained from DLS of M_0 when cycled from pH 7.4 to 4 and back to pH 7.4. Inset: Representative TEM image of M_0 after pH cycling (scale bar 100 nm). (d) Representative CLSM images of $^{f}M_0$ incubated with the ^{Rho}GUVs at pH 7.4 (left image) and after lowering the pH to 4 (right image) (scale bars 10 μm). Line scans across the selected ^{Rho}GUVs from the green channel (^{f}P1) and the red channel (^{Rho}PE) are shown at pH 7.4 (i) and after lowering the pH to 4 (ii).

hydrodynamic diameter (D_h) obtained from NTA measurements of 184 ± 41 nm (Figure S1a). (We would like to note that D_h was typically larger than sizes measured on TEM images that were recorded under high vacuum.) The critical micelle concentration (CMC) was 224 μg mL^{-1} (Figure 1b). This CMC value was comparable to the value reported for micelles made from polymers with the same hydrophobic PCMA block but with poly(2-(dimethylamino)ethyl methacrylate) as the hydrophilic extension[14] and slightly larger compared to micelles with poly(2-methacryloyloxyethyl phosphorylcholine) or polyethylene glycol methacrylate[41] as the hydrophilic part. Correlation curves of M_0 obtained from DLS at pH 7.4 and 4 as well as after neutralizing the sample back to pH 7.4 were rather similar (Figures 1c and S1b). A slight increase in size at pH 4 was observed compared to pH 7.4 due to the phase transition toward more hydrophobicity of the pH-sensitive PCEA, which was partially reversed when the pH was increased back to pH 7.4. TEM images of the samples after the pH cycle confirmed the structural integrity of M_0 (Figure 1c, inset) with a preserved size distribution (Figure S1c). Fluorescently labeled giant unilamellar vesicles (^{Rho}GUVs) were used to get the first insight into how Oregon Green-labeled M_0 ($^{f}M_0$), obtained by using ^{f}P1 for their assembly, interacted with a simple model lipid bilayer when incubated at pH 7.4 and after lowering of the environmental pH to 4 (Figure 1d). Confocal laser scanning microscopy (CLSM) images revealed that the polymer integrated into the lipid bilayer of the ^{Rho}GUVs at pH 7.4 after a short incubation time, illustrated by the overlapping intensity peaks of the red (^{Rho}PE) and green (^{f}P1) channels in the line scan (Figure 1di). It should be noted that the green signal of ^{f}P1 fainted upon the decrease in pH due to the dye's pH sensitivity. Nevertheless, the green signal could still be located in the membrane of the ^{Rho}GUVs when the pH dropped to 4 since the red and green signals still overlapped (Figure 1dii). Additionally, the number of intact ^{Rho}GUVs was reduced at pH 4. We concluded that this observation was due to the interaction of the pH responsive $^{f}M_0$ with the lipid bilayers and not due to the drop in pH itself because the ^{Rho}GUVs remained unaffected when the pH dropped in the absence of $^{f}M_0$ (Figure S1d). Moreover, $^{f}M_0$ did not seem to cross the lipid bilayer of the ^{Rho}GUVs at any of the tested pH values, since no fluorescent signal was observed in the aqueous void of the ^{Rho}GUVs.

Nanoformulations were previously equipped with the pH-sensitive amphiphilic peptide GALA, and their lysosomal escape ability was confirmed.[37,42] At a pH below 6, the abundantly present glutamic acids in the GALA peptide are protonated, provoking a switch to a helix formation and thereby making hydrophobic interactions with lipid membranes, such as the lysosomal membrane, possible.[43] Therefore, in order to implement a lysosomal escape strategy, GALA was covalently conjugated to the premade M_0 using an EDC/NHS coupling reaction, resulting in M_{GALA}. The NTA analysis revealed a minor aggregation of M_{GALA} compared to M_0 (Figure S2a), which was also reflected in a slightly higher PDI but similar hydrodynamic diameter (D_h) compared to those of the DLS measurements (Table S1). The successful GALA conjugation was confirmed by desalting and freeze-drying M_{GALA} followed by ^{1}H NMR analysis in DMSO-d_6. The peaks in the downfield region (Figure 2b, inset) originating from the aromatic amino acids histidine and tryptophan confirmed the presence of GALA peptide (Figure 2b). TEM images of M_{GALA} showed similar micellar assembles as M_0; i.e., the conjugation step did not affect the structural integrity of the micelles (Figure 2c). Similar to M_0, CLSM images showed that ^{f}P1 integrated into the lipid bilayer when $^{f}M_{GALA}$ was incubated with ^{Rho}GUVs at pH 7.4 and 4 (Figure 2di/ii). A noticeable difference in the interaction of $^{f}M_{GALA}$ with ^{Rho}GUVs compared to $^{f}M_0$ with ^{Rho}GUVs was that a higher amount of aggregated ^{Rho}GUVs already existed at pH 7.4, which increased at pH 4. The presence of GALA seemed to introduce stronger interactions between the ^{Rho}GUVs and $^{f}M_{GALA}$, and the conformational change as well as the more hydrophobic nature at low pH[43] resulted in a higher number of aggregated ^{Rho}GUVs. Nevertheless, $^{f}M_{GALA}$ did not visibly cross the lipid membrane of the ^{Rho}GUVs.

Hybrid Vesicle Assembly. The goal was to compare the same amphiphilic block copolymer P1 in micelles and as part of the HVs. We have previously successfully used P1 to

https://doi.org/10.1021/acs.biomac.1c01403
Biomacromolecules 2022, 23, 1052−1064

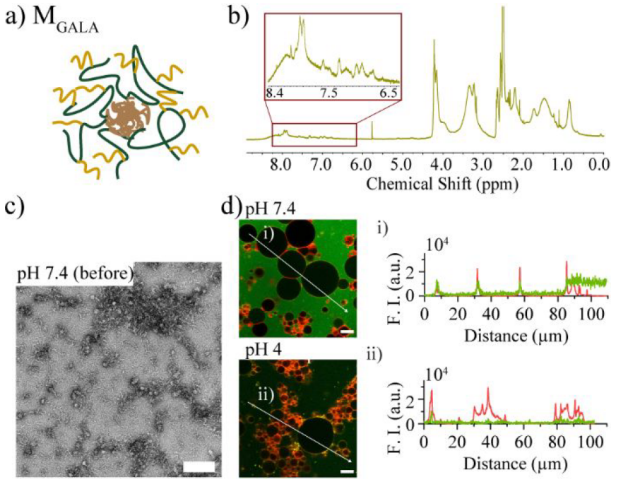

Figure 2. GALA-modified M_0 (M_{GALA}). (a) Cartoon illustrating M_{GALA}. (b) ^{1}H NMR spectrum of freeze-dried M_{GALA} dissolved in DMSO-d_6. (c) Representative TEM image of M_{GALA} (scale bar 200 nm). (d) Representative CLSM images of $^{f}M_{GALA}$ incubated with ^{Rho}GUVs at pH 7.4 (upper image) and after lowering the pH to 4 (lower image) (scale bars 10 μm). Line scans across the selected ^{Rho}GUVs from the green channel (^{f}P1) and the red channel (^{Rho}PE) are shown at pH 7.4 (i) and after lowering the pH to 4 (ii).

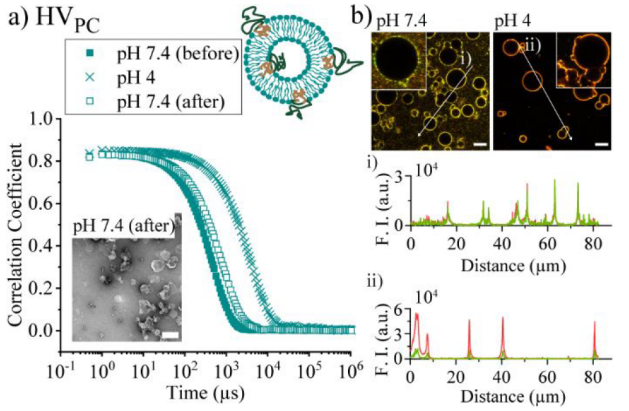

Figure 3. HV_{PC}. (a) Cartoon of HV_{PC} and the correlograms of HV_{PC} when cycled from pH 7.4 to 4 and back to pH 7.4 obtained from DLS. Inset: Representative TEM image of HV_{PC} after pH cycling (scale bar 200 nm). (b) Representative CLSM images of $^{f}HV_{PC}$ incubated with the GUVs at pH 7.4 (left image) and after lowering the pH to 4 (right image) (scale bars 10 μm). Inset: A close-up of a single GUV. Line scans across the selected GUVs from the green channel (^{f}P1) and the red channel (^{Rho}PE) are shown at pH 7.4 (i) and after lowering the pH to 4 (ii).

assemble the HVs with DOPC lipids.[40] Since we have shown that the HVs made with a similar amphiphilic block copolymer that had a hydrophilic extension of methionine methacryloyloxyethylester and 2-carboxyethyl acrylate did not have lysosomal escape abilities,[36] it was reasonable to assume that the pristine PCEA extension used here has a similar behavior. Therefore, we explored two options to integrate lysosomal escape properties by using either GALA-conjugated P1 or 1,2-dioleoyl-*sn*-glycero-3-phosphoethanolamine (DOPE) lipids for the HV assembly.

DOPC Lipid Containing HVs. HVs made of 0.4 mg of P1 and 1.1 mg of DOPC lipids were assembled on the basis of a prior reported protocol[40] using the film rehydration method, followed by extrusion through a 100 nm membrane and running over a size exclusion column to remove smaller polymeric assemblies and impurities. The obtained HVs are referred to as HV_{PC}. Their D_h and PDI from DLS and NTA measurements at pH 7.4 as well as the TEM images showed similar results to the previously reported hybrid vesicles (Figure 3a, Table S1, and Figure S3a,b).[40] The presence of both building blocks (^{f}P1 and ^{Rho}PE lipids) was confirmed by the two distinct peaks in the emission spectrum of $^{f}HV_{PC}$ (Figure S3c). Next, we tested the pH responsiveness of HV_{PC}. The correlation curve of HV_{PC} at pH 4 obtained from DLS indicated an increase in size and PDI due to the same reason outlined for M_0. This change was almost completely reversible when the pH was increased back to 7.4 (Figures 3a and S3d). We speculated that this observation was more likely due to the change in the optical density of the membrane as a result of the collapsed PCEA rather than vesicular aggregation. A comparison of the slopes of the correlograms at pH 7.4 and 4 revealed a slightly steeper slope for the latter, meaning that the polydispersity of the sample did not increase at the lower pH. This result supported the assumption that no major aggregates were formed, which would have yielded in a dramatic increase of the polydispersity. Moreover, the reversibility of aggregated samples would be expected to be less successful. TEM images of HV_{PC} after the pH titration confirmed the structural integrity of HV_{PC} (Figures 3a, inset and S3e). Additionally, the interaction of $^{f}HV_{PC}$ with the lipid bilayer of the GUVs was examined at pH 7.4 and 4 and after returning to pH 7.4 (Figures 3b and S3f). CLSM images at pH 7.4 revealed that $^{f}HV_{PC}$ interacted with the membranes of the nonlabeled GUVs, indicated by the yellow color originating from the overlap of the green (^{f}P1) and red (^{Rho}PE) signals of $^{f}HV_{PC}$, highlighting the membrane of the GUVs, which could also be observed in the line scans (Figure 3b). However, fluorescent signals of both ^{f}P1 and ^{Rho}PE were less homogeneously distributed in the membranes compared to when $^{f}M_0$ or $^{f}M_{GALA}$ were used, suggesting the existence of ^{f}P1 and ^{Rho}PE patches in the lipid bilayer. A decrease in the pH to 4 resulted in fewer GUVs, where the bigger GUVs disintegrated and smaller GUVs with a less patchy appearance of the lipid bilayer were maintained. This observation suggested that the pH-responsive polymer interfered with the structural integrity of the GUVs. However, the pH-dependent brightness of the Oregon Green dye might overexaggerate this effect. Nonetheless, the GUVs showed interesting aggregation behaviors at pH 4 due to the presence of $^{f}HV_{PC}$ represented by the GUVs seemingly fusing (Figure 3b, inset right image). Interestingly, only fluorescent signals originating from ^{Rho}PE were found in the membrane where the GUVs touch, suggesting that only the lipids were able to distribute in the membranes between the GUVs. Some of these events were also observed at pH 7.4 but not in the same abundancy as at pH 4. Therefore, we hypothesized that this was a pH-induced behavior mediated by the lipids' same nature in the GUVs and the HVs that allowed for mixing via lateral diffusion. Upon an increase of the pH back to 7.4, a higher amount of patches could be observed again, also due to the increased fluorescent intensity of ^{f}P1 at neutral pH (Figure S3f). The presence of the fused GUVs was preserved as well as the presence of ^{Rho}PE in the connecting lipid bilayer. No crossing of the GUV membrane by $^{f}HV_{PC}$ was observed at any of the pH values.

GALA-Conjugated HV_{PC} ($HV_{PC\text{-}GALA}$). Next, we aimed to equip HV_{PC} with the GALA peptides to obtain a comparable

https://doi.org/10.1021/acs.biomac.1c01403
Biomacromolecules 2022, 23, 1052−1064

vesicular assembly to M_{GALA}. In the first attempt, we conjugated the GALA peptide to the preformed HV_{PC}. This, however, led to disintegrated morphologies and aggregates, as shown in the NTA and TEM images (Figure S4a). Consequently, we decided to employ $P1_{GALA}$ for the assembly of $HV_{PC\text{-}GALA}$. However, since $P1_{GALA}$ was only soluble in DMSO, we could not use the rehydration method for the assembly as DMSO cannot be evaporated like THF due to its high boiling point. Therefore, an alternative HV assembling route was explored on the basis of the observations from the above outlined experiments where M_{GALA} was added to the GUVs and $^{f}P1_{GALA}$ integrated in the lipid bilayer of the GUVs. Additionally, the interaction and the incorporation of amphiphilic triblock copolymers with large unilamellar lipid vesicles had been investigated and shown.[44] The alternative HV assembly started with mixing DOPC liposomes with $^{f}P1_{GALA}$ (dissolved in DMSO), followed by dialysis to remove DMSO while $^{f}P1_{GALA}$ could integrate with the lipid bilayers before extrusion and purification. These HVs are referred to as $^{f}HV_{PC\text{-}GALA}$. TEM images of $^{f}HV_{PC\text{-}GALA}$ confirmed their vesicular nature and the absence of micelles (Figure 4a). The size distribution obtained from the NTA measurements and the TEM images was similar to that of HV_{PC} (Figure S4b,c). The fluorescence spectrum of $^{f}HV_{PC\text{-}GALA}$ confirmed the presence of both building blocks, although the peak for $^{f}P1_{GALA}$ was relatively low (Figure S4d). To ensure the formation of the HVs and that this alternative fabrication method still allowed for the encapsulation of cargo, we added 5(6)-carboxyfluorescein (CF) in a self-quenching concentration after the dialysis and before the extrusion, resulting in $^{CF}HV_{PC\text{-}GALA}$. For comparison, CF loaded DOPC liposomes ($^{CF}L_{PC}$) were prepared and the CF release from both vesicles was monitored over 120 h. The data were normalized to the maximum release upon disruption of the vesicles with Triton X (TX) at day 0. The initial higher release of CF from $^{CF}HV_{PC\text{-}GALA}$ compared to $^{CF}L_{PC}$ was another indication for the integration of $P1_{GALA}$ into the vesicles, which resulted in a higher permeability compared to a pristine lipid bilayer (Figure 4b), as shown in other examples.[32] Next, the pH responsiveness of $HV_{PC\text{-}GALA}$ was investigated by taking DLS correlograms at pH 7.4 and 4 and after an increase to pH 7.4 again. The curves only exhibited a slight shift toward increased time upon the pH decrease, which was almost reversed after cycling back to pH 7.4 (Figures 4c and S4e). The presence of GALA did not detectably change the pH behavior of the HVs. This observation was supported by the resemblance of the vesicles and their sizes in the TEM images before and after the pH drop and rise (Figures 4c and inset and S4f). The rather low fluorescence intensity of $^{f}HV_{PC\text{-}GALA}$ in the green channel led to a low intensity of green fluorescence in the CLSM images when investigating the interaction of $^{f}HV_{PC\text{-}GALA}$ with the GUVs (Figure 4d). However, the behavior of the GUVs upon addition of $^{f}HV_{PC\text{-}GALA}$ could be observed throughout the pH cycling, focusing on the fluorescent signal originating from ^{Rho}PE. The GUVs already aggregated at pH 7.4 upon the addition of $^{f}HV_{PC\text{-}GALA}$ with the integration of mostly ^{Rho}PE in the membranes of the GUVs without crossing the lipid membranes. A higher number of closely attached GUVs was observed upon the decrease of pH to 4, which was assumed to be a result of the enhanced interaction of the lipid bilayer with $^{f}P1$ and the GALA peptide. The attraction between $^{f}HV_{PC\text{-}GALA}$ and the GUVs was so strong that the spherical GUVs deformed to some extent without rupturing; additionally, there was potential partial fusion of their lipid bilayers. As expected, an increase in the pH back to 7.4 did not show any changes/reversibility (Figure S4g). It should be emphasized that there was a distinctly different interaction between $^{f}HV_{PC\text{-}GALA}$ or $^{f}HV_{PC}$ and the GUVs, confirming the presence of different types of HVs.

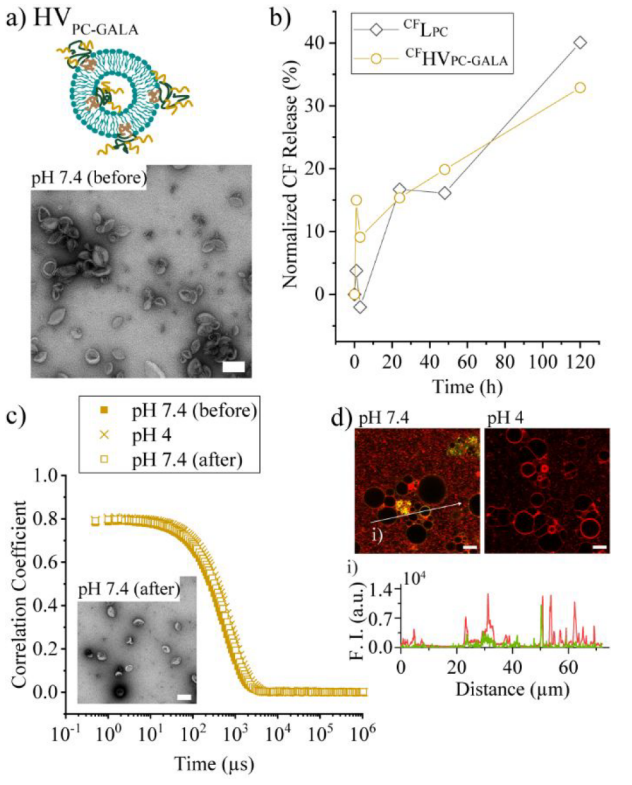

Figure 4. $HV_{PC\text{-}GALA}$. (a) Cartoon of $HV_{PC\text{-}GALA}$ and representative TEM image of $HV_{PC\text{-}GALA}$ (scale bar 200 nm). (b) Normalized 5(6)-carboxyfluorescein (CF) release from $^{CF}HV_{PC\text{-}GALA}$ and $^{CF}L_{PC}$ over 120 h. (c) Correlograms of $HV_{PC\text{-}GALA}$ when cycled from pH 7.4 to 4 and back to pH 7.4 obtained from DLS. Inset: Representative TEM image of $HV_{PC\text{-}GALA}$ after pH cycling (scale bar 200 nm). (d) Representative CLSM images of $^{f}HV_{PC\text{-}GALA}$ incubated with the GUVs at pH 7.4 (left image) and after lowering the pH to 4 (right image) (scale bars 10 μm). Line scans across the selected GUVs from the green channel ($^{f}P1$) and the red channel (^{Rho}PE) at pH 7.4 are shown.

For comparison, liposomes consisting of DOPC lipids and 9 mol % cholesterol were assembled and referred to as L_{PC}. This amount of cholesterol was chosen because it corresponded to the quantity of cholesterol incorporated in HV_{PC}. The D_h from DLS and NTA and the size distribution from the TEM images of L_{PC} were similar to those of HV_{PC} (Figure S5a,b). As expected, due to the absence of any pH-responsive groups, there was no shift in the correlograms when cycling the pH from 7.4 to 4 and back to 7.4, which was also confirmed by the structural integrity of the vesicles in the TEM images and their size distribution after pH cycling (Figure S5c and inset). When Rho-labeled $^{Rho}L_{PC}$ was added to the unlabeled GUVs, black round shaped areas appeared in the red background of the signal originating from ^{Rho}PE of $^{Rho}L_{PC}$ (Figure S5d). This observation indicated that the presence of P1 favored the integration or interaction with the lipid bilayer of the GUVs while pure lipid−cholesterol vesicles only showed this

https://doi.org/10.1021/acs.biomac.1c01403
Biomacromolecules 2022, 23, 1052−1064

association weakly after some time. Upon lowering the pH to 4, more of the ^{Rho}PE integrated into the membranes of the GUVs, revealing homogeneously red colored GUVs. The Rho label fainted due to pH sensitivity; but at the same time, the GUVs were largely unaffected in number and no severe aggregation was observed. This appearance did not change further when the pH was increased back to around 7.4 (Figure S5f). Consequently, the earlier findings of the interactions and the incorporation of polymer into the lipid bilayer of the GUVs were mediated by the pH-responsive P1 and/or the GALA peptide.

DOPE-Containing HVs (HV_{PE}). DOPE lipids are often incorporated in lipid-based formulations as helper lipids for intracellular DNA or mRNA delivery in lipoplexes.[45] The smaller headgroup of DOPE compared to DOPC increases the tendency of DOPE to form inverted hexagonal structures, whereas a formation of vesicles is only possible at a pH above 8. This phase transition can be further tuned to lower pH values by the addition of either other lipids or a block copolymer, as in our case. The switch in the integrity of the vesicles promotes the destabilization of the endosomal/lysosomal membranes and can therefore be used as an endosomal/lysosomal escape strategy.[45−47]

Here, HVs were assembled by the film rehydration method using 0.4 mg of P1 and 1.1 mg of DOPE lipids followed by extrusion through 100 nm membranes and running through a size exclusion column. The obtained HVs are referred to as HV_{PE}. The TEM images of HV_{PE} revealed the vesicular morphology with a fraction of small-sized micelle-like assemblies (Figure 5a) and a size distribution of 245 ± 129 nm determined from the TEM images (Figure S6b). The NTA measurement illustrated a narrow population of assemblies with a D_h of ∼177 nm (Figure S6a), and the emission spectrum confirmed the presence of both building blocks (Figure S6c). It should be noted that DOPE lipids with 9 mol % cholesterol (corresponding to the amount of cholesterol in P1) did not yield vesicles but only aggregates (Figure S6d), illustrating that the presence of P1 facilitated and stabilized the assembly of the HVs. The ability of polymers to stabilize DOPE-containing vesicles has previously been observed when, for instance, the temperature-responsive polymer poly(*N*-isopropylacrylamide-*co*-*N*,*N*′-dimethylaminopropylacrylamide) was conjugated to DOPE.[48] The pH responsiveness of HV_{PE} was an important aspect to consider since structural changes in the HVs, due to the acidification in the lysosomes, are expected to contribute to the escape from these organelles. The correlograms obtained from DLS for HV_{PE} shifted to longer times that corresponded to an increase in size and PDI when the pH was lowered from 7.4 to 4 (Figures 5b and S6e). Unlike HV_{PC}, no recovery was observed upon increasing the pH back to 7.4 for HV_{PE}, suggesting a structural change of the assemblies, which was not caused by the reversible pH-induced collapse of PCEA. DLS data of a stepwise decrease of the pH from 7.4 to 4 revealed that the loss of the structural integrity of HV_{PE} occurred at a pH of around 6 in the form of increased D_h and PDI (Figure S6f). This transition pH corresponds to the environmental pH in the early endosome during the process of endocytosis. Further, the membrane permeability and consequential cargo retention and release are important characteristics of vesicle-based carriers. Therefore, Laurdan was used as a fluorescent probe to assess the packing of the membrane of HV_{PE} (Figure 5c). The calculated general polarity (GP) of HV_{PE} was 0.1 ± 0.03, which was ∼0.35 larger

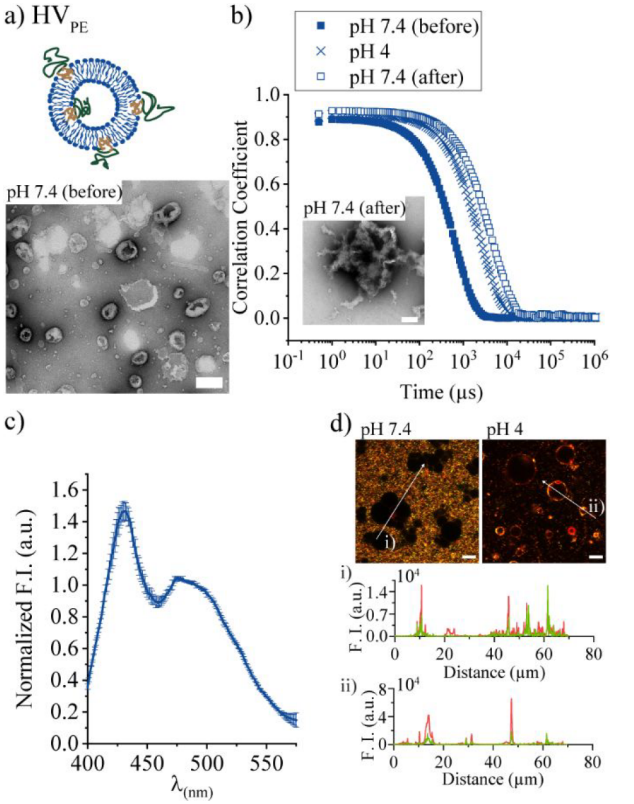

Figure 5. HV_{PE}. (a) Cartoon of HV_{PE} and representative TEM image of HV_{PE} (scale bar 200 nm). (b) Correlograms obtained from DLS of HV_{PE} when pH was lowered from 7.4 to 4 and increased back to pH 7.4. Inset: representative TEM image of HV_{PE} after pH cycling (scale bar 200 nm). (c) Fluorescent emission spectra (λ_{ex} = 340 nm, λ_{em} = 380−600 nm) of HV_{PE} using Laurdan as a probe for membrane polarity (normalized to F.I. at λ_{em} = 490 nm). (d) Representative CLSM images of $^{f}HV_{PE}$ incubated with the GUVs at pH 7.4 (left image) and after lowering the pH to 4 (right image) (scale bars 10 μm). Line scans across the selected GUVs from the green channel (^{f}P1) and the red channel (^{Rho}PE) are shown at pH 7.4 (i) and after lowering the pH to 4 (ii).

compared to previously reported GP values for HV_{PC} and L_{PC},[40] indicating a stiffer membrane. This result could be explained by the more dense packing and higher association of DOPE lipids with P1 in order to maintain a vesicular morphology, resulting in a decreased lateral diffusion and lower water penetration.[46] Finally, when exposing $^{f}HV_{PE}$ to the GUVs at pH 7.4, CLSM images revealed no visible interaction of either ^{f}P1 or ^{Rho}PE with the lipid bilayers of the GUVs (Figure 5d). The GUVs could be observed as round shaped black areas with no highlighted outline as that seen for HV_{PC}. However, when the pH was decreased to 4, an obvious red signal, as well as a faint green signal, could be observed in the GUVs' lipid bilayers. Both signals formed patches in the GUVs' membrane at the time of the observation, suggesting the incorporation of ^{f}P1 and ^{Rho}PE when the amphiphilic nature of the block copolymer turned to a mostly hydrophobic state and DOPE destabilized the vesicles. Additionally, the GUVs with homogeneously distributed ^{Rho}PE and minimal ^{f}P1 were found. Overall, the GUVs were less aggregated compared to the exposure to $^{f}HV_{PC\text{-}GALA}$, indicating the different types of the HVs interact differently with the GUVs as expected. No reversibility of ^{Rho}PE or ^{f}P1 incorporation in the lipid bilayer of

https://doi.org/10.1021/acs.biomac.1c01403
Biomacromolecules 2022, 23, 1052−1064

the GUVs was observed when the pH was increased to 7.4 (Figure S6g).

Biological Evaluation. We aimed to compare the short-term toxicity, the uptake efficacy, and the intracellular fate of the different assemblies in macrophage-like murine RAW 264.7 cells (RAW cells for short) to understand the effect of the same building block made into different assemblies on the cells, i.e., P1 assembled as micelles or as the polymeric building block in the HVs. L_{PC} was used for comparison. Although not human derived, RAW cells are a model for the initial screening of diverse (nano)materials and compounds to help predict their toxicity or bioactivity in primary cells. Macrophage-like cells were chosen since they are typically the first cells that encounter non-native moieties entering an organism.

Interaction of Micelles with RAW Cells. First, we evaluated the 24 h short-term toxicity of M_0 and M_{GALA} in RAW cells that confirmed the preserved viability of the cells for the tested concentrations and time (Figure 6a). Interestingly, the cell viability seemed to increase to a higher level in the presence of M_0, suggesting more metabolically active cells when incubated with the micelles due to a higher cellular dehydrogenase activity that was assessed using CCK-8. Similarly, the viability of RAW cells seemingly increased when the mitochondrial dehydrogenase activity was detected using the MTT assay (Figure S8a). Complementarily, when using the LDH assay, no differences were observed as compared to the untreated cells, suggesting no interference with the cell membrane integrity (Figure S8b). M_{GALA} had a similar trend when using the CCK-8 assay, but the higher micelle concentration suggested an onset of minor toxicity indicated by a decrease in the detected cell viability following the initial increase to ~180%. Second, the uptake efficacy of $^{f}M_0$ and $^{f}M_{GALA}$ after 3, 6, and 24 h was assessed by flow cytometry (Figure 6b). As expected, the normalized cell mean fluorescence (nCMF) increased significantly over time due to the associated $^{f}M_0$ and $^{f}M_{GALA}$. While after 6 h of incubation, no difference in nCMF was found between $^{f}M_0$ and $^{f}M_{GALA}$, a 24 h incubation time resulted in a statistically significant higher nCMF for $^{f}M_{GALA}$. Third, the intracellular fate of the two assemblies was evaluated by replacing the micelle-containing media after 6 h with pristine media, and the cells were incubated for an additional 18 h before monitoring the CMF by flow cytometry (Figure 6c). For both micelles, the nCMF dropped significantly down to 75% of the starting value within the 18 h of resting time, suggesting that the cells processed the micelles and/or they were exocytosed. The latter aspect was supported by measuring the fluorescent intensity of phenol red free cell media after the 18 h of resting time without $^{f}M_0$ (Figure S8c). Higher fluorescent intensities originating from ^{f}P1 were found in the cell media when increasing amounts of $^{f}M_0$ were initially added to the RAW cells, suggesting exocytosis. However, only below 10% of the maximum attainable fluorescent intensity, i.e., the fluorescent intensity measured when the corresponding amount of $^{f}M_0$ was added to phenol red free cell media, was detected. It should be noted that this comparison might have been affected by $^{f}M_0$ sticking to the surface of the wells. Finally, the ability of $^{f}M_0$ and $^{f}M_{GALA}$ to escape the endosomes/lysosomes was compared. To this end, the cells were incubated with the micelles for 6 h followed by 18 h in fresh media before staining of the lysosomes and cell membranes for visualization by CLSM (Figures 6d and S8d,e for split channels). $^{f}M_0$ and $^{f}M_{GALA}$ were internalized by the cells during the incubation time as indicated by the origin of the entire fluorescent signals from inside of the stained cell membrane (light gray). Moreover, the cyan color in the images, a result of the overlapping of green $^{f}M_0$ and blue lysosomes, suggested that $^{f}M_0$ remained trapped in the lysosomes (Figure 6di). In contrast, the green signals from $^{f}M_{GALA}$ were less confined and only associated with more faint blue lysosome signals (Figure 6dii). The lower intensities of the lysotracker signal suggested impairment of the lysosomes and probable leakage, resulting in a less acidic environment due to a partial escape of the micelles from the endosomes/lysosomes facilitated by the GALA peptide. A more homogeneous distribution of $^{f}M_{GALA}$ throughout the cytosol compared to $^{f}M_0$ was observed when considering only the green channel, which supported the indication of lysosomal escape (Figure S7a). In order to semiquantify the escape efficacy, the Manders correlation coefficient (MCC) was calculated.[49] The resulting MCC of ~0.7 (0.69 ± 0.21 and 0.72 ± 0.12) for both $^{f}M_0$ and $^{f}M_{GALA}$ colocalized with the lysosomes did not reflect the differences observed in the images of the two samples. However, an MCC of 0.79 ± 0.26 and 0.45 ± 0.14 was calculated when considering the

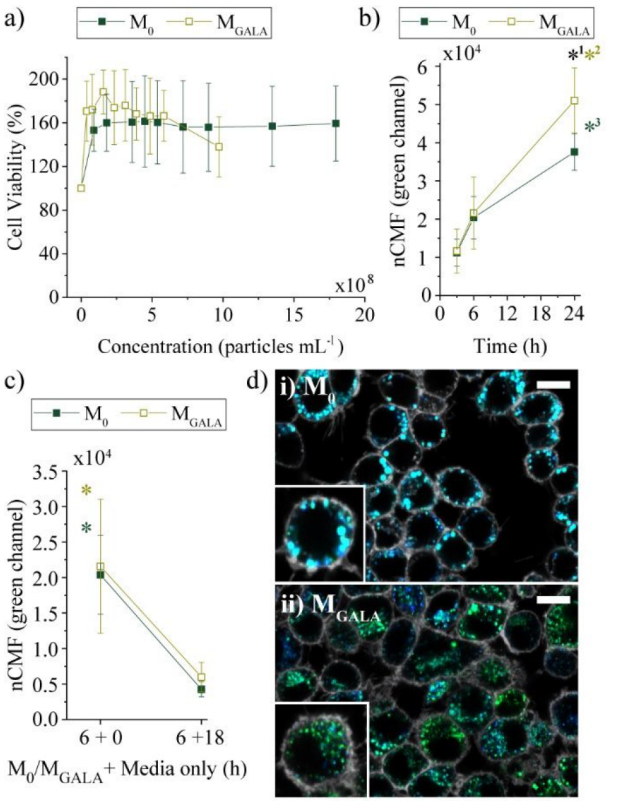

Figure 6. Interaction of M_0 and M_{GALA} with RAW cells. (a) Viability of the RAW cells after incubation with M_0 or M_{GALA} for 24 h. (b) Normalized cell mean fluorescence (nCMF) of the RAW cells after exposure to $^{f}M_0$ and $^{f}M_{GALA}$ for 3, 6, or 24 h (n = 3, *p < 0.077: (1) M_{GALA} compared to M_0 at 24 h; *p < 0.05: (2) M_{GALA} at 24 h compared to itself at 6 and 3 h and (3) M_0 at 24 h compared to itself at 6 and 3 h). (c) nCMF of the RAW cells after incubation with $^{f}M_0$ or $^{f}M_{GALA}$ for 6 h and followed by incubation for 18 h in media (n = 3, *p < 0.05 comparing the two different points within the same sample). (d) Representative CLSM images of the cells incubated with $^{f}M_0$ (i) or $^{f}M_{GALA}$ (ii) for 6 h (green: $^{f}M_0$ or $^{f}M_{GALA}$; blue: LysoTracker Red DND-99 stained lysosomes; light gray: CellMask Deep Red Plasma Membrane Stain) (scale bars 10 μm).

https://doi.org/10.1021/acs.biomac.1c01403
Biomacromolecules 2022, 23, 1052−1064

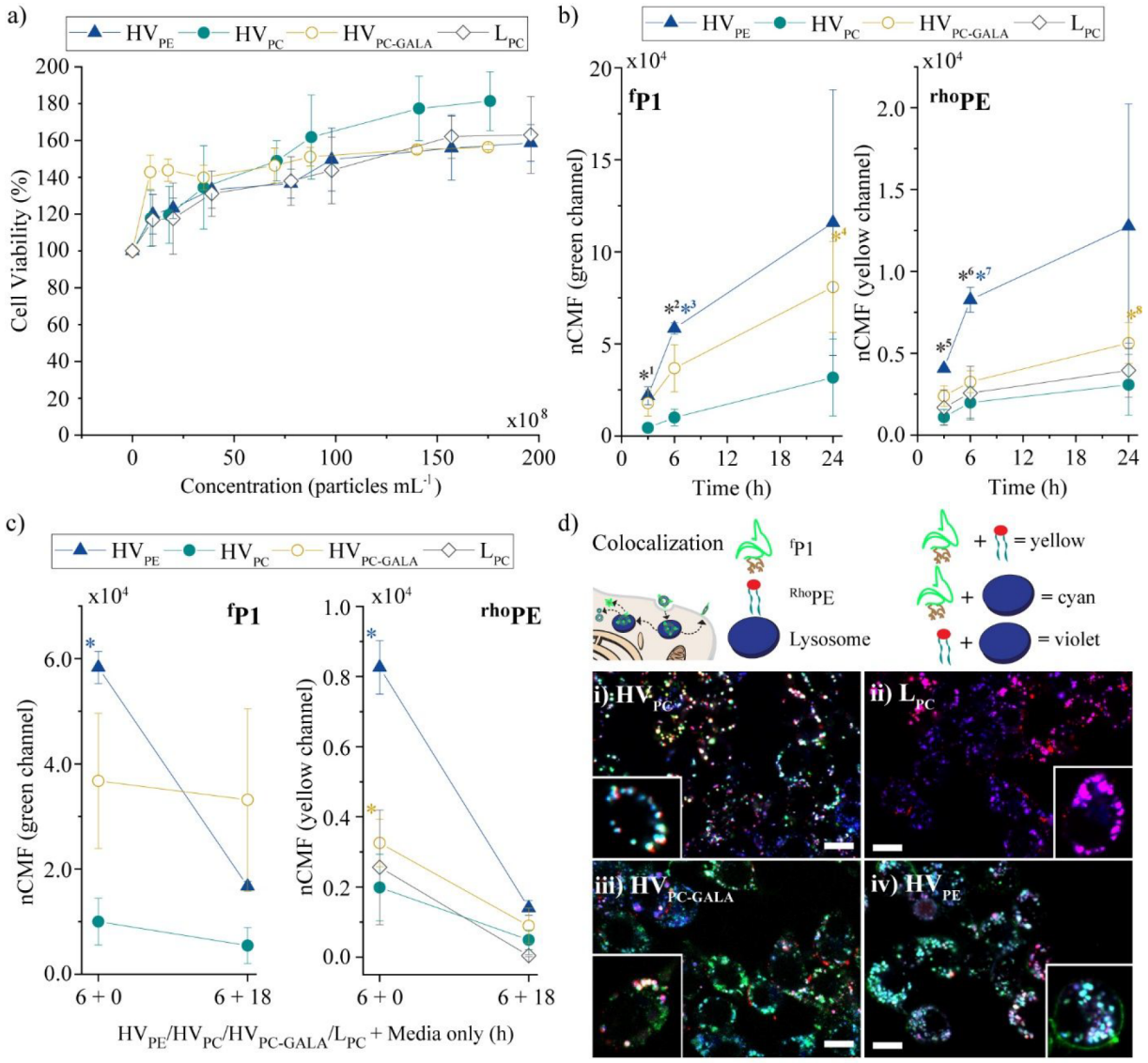

Figure 7. Interaction of the HVs with RAW cells. (a) Cell viability of RAW cells after incubation with HV_{PE}, HV_{PC}, $HV_{PC\text{-}GALA}$, or L_{PC} for 24 h. (b) Normalized cell mean fluorescence (nCMF) of RAW cells after exposure to ${}^{f}HV_{PE}$, ${}^{f}HV_{PC}$, ${}^{f}HV_{PC\text{-}GALA}$, or ${}^{Rho}L_{PC}$ for 3, 6, or 24 h (^{f}P1: green channel; ^{Rho}PE: yellow channel; $n = 3$, $*p < 0.05$ comparing in the green channel: (1) HV_{PC} to the others at 3 h, (2) all the samples compared to each other at 6 h, (3) HV_{PE} at 6 to 3 h within the same sample, and (4) $HV_{PC\text{-}GALA}$ at 24 to 3 h within the same sample; comparing in the yellow channel: (5/6) HV_{PE} to the others at the same time point, (7) HV_{PE} at 6 to 3 h within the same sample, and (8) $HV_{PC\text{-}GALA}$ at 24 h to the other time points of the same sample). (c) nCMF of RAW cells after exposure to ${}^{f}HV_{PE}$, ${}^{f}HV_{PC}$, ${}^{f}HV_{PC\text{-}GALA}$, or ${}^{Rho}L_{PC}$ for 6 and 18 h with fresh media (^{f}P1: green channel; ^{Rho}PE: yellow channel; $n = 3$, $*p < 0.05$ comparing the two different time points within the same samples). (d) Representative CLSM images of RAW cells incubated with ${}^{f}HV_{PC}$, ${}^{Rho}L_{PC}$, ${}^{f}HV_{PC\text{-}GALA}$, or ${}^{f}HV_{PE}$ for 24 h (green: ^{f}P1; red: ^{Rho}PE; blue: LysoTracker Deep Red) (scale bars 10 μm).

colocalization of the lysosomal fraction with ${}^{f}M_0$ and ${}^{f}M_{GALA}$, respectively. This result supported our assumption that, generally, higher amounts of empty or disrupted and thus more diffused lysosomes were present in cells that were incubated with ${}^{f}M_{GALA}$ compared to ${}^{f}M_0$ due to the interaction of ${}^{f}M_{GALA}$ with the lysosomal membranes.

Interaction of Vesicles with RAW Cells. First, the absence of 24 h short-term toxicity of the RAW cells incubated with HV_{PE}, HV_{PC}, $HV_{PC\text{-}GALA}$, or L_{PC} was confirmed (Figure 7a). In contrast to the incubation with micelles, the RAW cell viability seemed to increase with higher concentrations of vesicles, probably due to enhanced metabolism. Complementary, the RAW cells exposed to HV_{PC} were assessed using the MTT assay and LDH assay, and no differences to the untreated cells were found (Figure S9a,b). This observation supported the assumption that the internalization of the vesicles affected the cellular dehydrogenases, but neither the performance of the mitochondrial dehydrogenases nor the cell membrane integrity was changed. The uptake efficacy of the fluorescently labeled HVs (${}^{f}HV_{PC}$, ${}^{f}HV_{PC\text{-}GALA}$, and ${}^{f}HV_{PE}$) and ${}^{Rho}L_{PC}$ after 3, 6, and 24 h was assessed by monitoring the green and yellow channels to follow ^{f}P1 and ^{Rho}PE, respectively (Figure 7b). Since the same particle concentrations of micelles/vesicles were incubated with the RAW cells and the read-out was normalized to the fluorescent intensity of the assemblies, a comparison between them was possible. As expected, the nCMF had an increasing trend over time due to the associated HVs and ${}^{Rho}L_{PC}$. Only RAW cells incubated with ${}^{f}HV_{PE}$ showed a

https://doi.org/10.1021/acs.biomac.1c01403
Biomacromolecules 2022, 23, 1052−1064

statistically significant increase over 6 h in the green and yellow channels. Incubation with the other vesicles resulted in a statistically significant lower increase in the green channel and especially in the yellow channel at 3 and 6 h compared to HV_{PE}, leading to the assumption that HV_{PE} possesses the highest uptake efficacy of these assemblies. $^{f}HV_{PC\text{-}GALA}$ also showed a significantly higher association with the RAW cells than $^{f}HV_{PC}$ in the green channel, supporting the difference in the uptake for $^{f}M_{GALA}$ versus $^{f}M_{0}$ and the suggestion that $^{f}P1_{GALA}$ increases uptake efficacy compared to $^{f}P1$. $^{f}HV_{PC}$ and $^{Rho}L_{PC}$ had the lowest association with the RAW cells, which was not surprising since the slightly negative or the zwitterionic nature of the hybrid vesicles or the liposomes limited their interaction with the RAW cells.[50]

The intracellular fate of the vesicles was evaluated by replacing the vesicle-containing media with pristine media after 6 h, and the RAW cells were incubated for an additional 18 h before monitoring the CMF by flow cytometry in the green and yellow channels (Figure 7c). For all types of vesicles, the nCMF in the yellow channel dropped to between 17% and 27% of the starting value within the 18 h resting time, suggesting that the cells processed the lipids. On the other hand, the fluorescent signal originating from $^{f}P1$ (green channel) remained at a comparable level when HV_{PC} and $HV_{PC\text{-}GALA}$ were used but statistically significantly dropped in the case of HV_{PE}. This observation illustrated that the same block copolymer formulated with different types of lipids alters how the cells processed the assemblies.

Finally, the ability of the vesicles to escape the endosomes/lysosomes was compared. To this end, RAW cells were incubated with the vesicles for 24 h before staining the lysosomes for visualization using CLSM (Figures 7d and S9c−f for split channels). The CLSM images showed that both $^{f}HV_{PC}$ and $^{Rho}L_{PC}$ remained trapped in the lysosomes due to the overlapping signals originating from the fluorescent labels in $^{f}HV_{PC}$ (green: $^{f}P1$; red: ^{Rho}PE) or $^{Rho}L_{PC}$ (red: ^{Rho}PE) and the stained lysosomes (blue). (The colocalization of the two building blocks of the HVs resulted in a yellow color (overlapping green and red), while the green $^{f}P1$ signal and the red ^{Rho}PE signal overlap with blue lysosomes to form cyan and violet, respectively.) In other words, all fluorescent signals were overlapping apart from the occasional lysotracker signals (blue), indicating empty lysosomes. Similarly, the dominant color in the images of cells exposed to $^{Rho}L_{PC}$ was violet, confirming the inability of pristine liposomes to escape the endosomes/lysosomes. The few spots with only red signals from ^{Rho}PE were in close proximity to the cell membrane, which were assumed to be internalized $^{Rho}L_{PC}$ but before the acidification of the endosomes. In contrast, the fluorescent signals from $^{f}HV_{PC\text{-}GALA}$ and $^{f}HV_{PE}$ were less confined and more delocalized from the blue lysosomes. A similarly dispersed green $^{f}P1_{GALA}$ signal was found for cells incubated with $^{f}HV_{PC\text{-}GALA}$ or $^{f}M_{GALA}$, which was obvious when considering the green channel only (Figure S7aii,bii). Interestingly, patches of green fluorescence were observed in the cell membrane when $^{f}HV_{PE}$ was used, suggesting that (part of) $^{f}P1$ ended up in the cell membrane presumably when the early endosomes were formed, while ^{Rho}PE was trapped in the endosomes/lysosomes. Further, lysosomes in RAW cells incubated with $^{f}HV_{PE}$ or $^{f}HV_{PC\text{-}GALA}$ were seemingly larger compared to the smaller and confined fluorescent signals from the lysosomes of RAW cells exposed to $^{f}HV_{PC}$ or $^{Rho}L_{PC}$ as well as $^{f}M_{0}$ and $^{f}M_{GALA}$. This was an unexpected observation that pointed toward differences in the cellular process depending on the composition of the vesicles. The MCC was calculated to obtain a semiquantitative lysosomal escape efficacy. However, the resulting MCC of the colocalization of $^{f}P1$ or ^{Rho}PE with the lysosomes was between 0.6 and 0.9 in all the cases (details in Table S2), which insufficiently reflected the observed differences in the CLSM images. We speculated that this mismatch might be due to the fact that many images with more diffused signals originating from $^{f}P1$ also had a seemingly more diffused and faint signal from the lysotracker, resulting in the algorithm considering them as colocalized. This situation was most severe for RAW cells incubated with $^{f}HV_{PE}$ or $^{f}HV_{PC\text{-}GALA}$, suggesting that the escaping polymer might have been associated with the lysotracker. Nevertheless, the MCC of the fraction of lysosomes colocalized with either $^{f}P1$ or ^{Rho}PE was between 0.3 and 0.6 with typically lower values for ^{Rho}PE, especially in the case of $^{f}HV_{PC\text{-}GALA}$ (details in Table S2). This observation pointed toward a higher number of lysosomes colocalized with $^{f}P1$ than with ^{Rho}PE, which could be explained by assisted escape or the faster degradation of ^{Rho}PE.

CONCLUSIONS

We report the assembly and characterization of pH-responsive polymeric micelles and polymer−lipid HVs as different model systems for structural scaffolds as artificial organelles and their interaction with RAW 264.7 cells. Their individually differing pH-dependent incorporation and interaction with the GUVs demonstrated that the interaction of zwitterionic lipid bilayers with pH-responsive assemblies was dependent on their compositions. No short-term cytotoxicity was observed in RAW cells for all the assemblies. GALA peptide conjugated to the amphiphilic block copolymer indicated increased uptake efficacy, higher retention rates, and increased lysosomal escape capabilities in the RAW cells compared to the alternatives.

This effort provides insight into how cells interact with the different building blocks as potential scaffolds for artificial organelles; i.e., the intracellular retention and the intracellular structural integrity of the assemblies were very low. Consequently, further studies need to address these challenges in order to obtain structurally intact and functional soft material-based artificial organelles. Cross-linking of the assembled building blocks would give more insights into the possibilities of the cytosolic placement of intact vesicular assemblies in mammalian cells. The improvement of intracellular retention is a rarely explored challenge since the accumulation of carriers in nanomedicine is typically not desired. Modifications that will make the synthetic moieties more acceptable by the cell will be required, taking the observed improvement for the GALA-conjugated assemblies as a starting point.

ASSOCIATED CONTENT

Supporting Information

The Supporting Information is available free of charge at https://pubs.acs.org/doi/10.1021/acs.biomac.1c01403.

Details of micelle, HV, and L_{PC} characterization (NTA, DLS, correlograms, fluorescent emission spectra, TEM images, and size distributions); CLSM images of the ^{Rho}GUVs only at pH 7 and 4; CLSM images of the vesicles with the GUVs at pH 7.4 after pH cycling; CLSM images and line scans of the interaction of $^{Rho}L_{PC}$

https://doi.org/10.1021/acs.biomac.1c01403
Biomacromolecules 2022, 23, 1052−1064

and the GUVs at pH 7.4 and 4 and after the increase to pH 7.4; MTT and LDH assay data of RAW 264.7 cells incubated with M_0 and HV_{PC}; fluorescent intensity of cell media after incubation of RAW 264.7 cells with $^{f}M_0$; split channels of CLSM images of RAW 264.7 cells incubated with micelles and vesicles; details on MCC values for colocalization of vesicles and lysosomes (PDF)

AUTHOR INFORMATION

Corresponding Author

Brigitte Städler − *Interdisciplinary Nanoscience Center (iNANO), Aarhus University, 8000 Aarhus, Denmark;* orcid.org/0000-0002-7335-3945; Email: bstadler@inano.au.dk

Authors

Carina Ade − *Interdisciplinary Nanoscience Center (iNANO), Aarhus University, 8000 Aarhus, Denmark;* orcid.org/0000-0002-1467-1185

Xiaomin Qian − *Interdisciplinary Nanoscience Center (iNANO), Aarhus University, 8000 Aarhus, Denmark;* orcid.org/0000-0002-2598-0661

Edit Brodszkij − *Interdisciplinary Nanoscience Center (iNANO), Aarhus University, 8000 Aarhus, Denmark;* orcid.org/0000-0002-4911-1604

Paula De Dios Andres − *Interdisciplinary Nanoscience Center (iNANO), Aarhus University, 8000 Aarhus, Denmark*

Järvi Spanjers − *Interdisciplinary Nanoscience Center (iNANO), Aarhus University, 8000 Aarhus, Denmark*

Isabella N. Westensee − *Interdisciplinary Nanoscience Center (iNANO), Aarhus University, 8000 Aarhus, Denmark;* orcid.org/0000-0003-4895-0964

Complete contact information is available at: https://pubs.acs.org/10.1021/acs.biomac.1c01403

Notes

The authors declare no competing financial interest.

The raw/processed data required to reproduce these findings are available to download from https://sciencedata.dk/shared/5a6ee2bbe572fed58c544bf3e396687c.

ACKNOWLEDGMENTS

Independent Research Fund Denmark, Technology and Production Sciences (Project No. 8022-00159B) is acknowledged for funding. This project was supported by the European Research Council (ERC) under the European Union's Horizon 2020 research and innovation programme (grant agreement No. 818890). E.B. has received funding from the European Union's Horizon 2020 research and innovation programme under the Marie Skłodowska-Curie grant agreement No. 842640. The authors thank Associate Prof. Kenneth Howard (Aarhus University, Denmark) for access to the Nanosight LM-10 instrument.

REFERENCES

(1) Qian, X.; Nymann Westensee, I.; Brodszkij, E.; Städler, B. Cell Mimicry as a Bottom-up Strategy for Hierarchical Engineering of Nature-Inspired Entities. *WIREs Nanomed. Nanobiotechnol.* **2021**, *13*, e1683.

(2) Elani, Y. Interfacing Living and Synthetic Cells as an Emerging Frontier in Synthetic Biology. *Angew. Chem., Int. Ed.* **2021**, *60*, 5602−5611.

(3) Oerlemans, R. A. J. F.; Timmermans, S. B. P. E.; van Hest, J. C. M. Artificial Organelles: Towards Adding or Restoring Intracellular Activity. *Chembiochem* **2021**, *22*, 2051−2078.

(4) Simmel, F. C. Synthetic Organelles. *Emerg. Top Life Sci.* **2019**, *3*, 587−595.

(5) Mukerabigwi, J. F.; Ge, Z.; Kataoka, K. Therapeutic Nanoreactors as In Vivo Nanoplatforms for Cancer Therapy. *Chem.—Eur. J.* **2018**, *24*, 15706−15724.

(6) Peters, R. J. R. W.; Louzao, I.; van Hest, J. C. M. From Polymeric Nanoreactors to Artificial Organelles. *Chem. Sci.* **2012**, *3*, 335−342.

(7) Zhang, Y.; Gal, N.; Itel, F.; Westensee, I. N.; Brodszkij, E.; Mayer, D.; Stenger, S.; Castellote-Borrell, M.; Boesen, T.; Tabaei, S. R.; Höök, F.; Städler, B. Hybrid Vesicles as Intracellular Reactive Oxygen Species and Nitric Oxide Generators. *Nanoscale* **2019**, *11*, 11530−11541.

(8) Zhao, R.; Liu, X.; Yang, X.; Jin, B.; Shao, C.; Kang, W.; Tang, R. Nanomaterial-Based Organelles Protect Normal Cells against Chemotherapy-Induced Cytotoxicity. *Adv. Mater.* **2018**, *30*, 1801304.

(9) Belluati, A.; Craciun, I.; Palivan, C. G. Bioactive Catalytic Nanocompartments Integrated into Cell Physiology and Their Amplification of a Native Signaling Cascade. *ACS Nano* **2020**, *14*, 12101−12112.

(10) Tanner, P.; Balasubramanian, V.; Palivan, C. G. Aiding Nature's Organelles: Artificial Peroxisomes Play Their Role. *Nano Lett.* **2013**, *13*, 2875−2883.

(11) Lin, Y.-H.; Chen, Y.-P.; Liu, T.-P.; Chien, F.-C.; Chou, C.-M.; Chen, C.-T.; Mou, C.-Y. Approach To Deliver Two Antioxidant Enzymes with Mesoporous Silica Nanoparticles into Cells. *ACS Appl. Mater. Interfaces* **2016**, *8*, 17944−17954.

(12) Larrañaga, A.; Isa, I. L. M.; Patil, V.; Thamboo, S.; Lomora, M.; Fernández-Yague, M. A.; Sarasua, J.-R.; Palivan, C. G.; Pandit, A. Antioxidant Functionalized Polymer Capsules to Prevent Oxidative Stress. *Acta Biomater.* **2018**, *67*, 21−31.

(13) Pavlovic, M.; Muráth, S.; Katona, X.; Alsharif, N. B.; Rouster, P.; Maléth, J.; Szilagyi, I. Nanocomposite-Based Dual Enzyme System for Broad-Spectrum Scavenging of Reactive Oxygen Species. *Sci. Rep.* **2021**, *11*, 4321.

(14) Ade, C.; Brodszkij, E.; Thingholm, B.; Gal, N.; Itel, F.; Taipaleenmäki, E.; Hviid, M. J.; Schattling, P. S.; Städler, B. Small Organic Catalase Mimic Encapsulated in Micellar Artificial Organelles as Reactive Oxygen Species Scavengers. *ACS Appl. Polym. Mater.* **2019**, *1*, 1532−1539.

(15) Shah, J.; Pandya, A.; Goyal, P.; Misra, S. K.; Singh, S. BSA-Decorated Magnesium Nanoparticles for Scavenging Hydrogen Peroxide from Human Hepatic Cells. *ACS Appl. Nano Mater.* **2020**, *3*, 3355−3370.

(16) van Oppen, L. M. P. E.; Abdelmohsen, L. K. E. A.; van Emst-de Vries, S. E.; Welzen, P. L. W.; Wilson, D. A.; Smeitink, J. A. M.; Koopman, W. J. H.; Brock, R.; Willems, P. H. G. M.; Williams, D. S.; van Hest, J. C. M. Biodegradable Synthetic Organelles Demonstrate ROS Shielding in Human-Complex-I-Deficient Fibroblasts. *ACS Cent. Sci.* **2018**, *4*, 917−928.

(17) Einfalt, T.; Witzigmann, D.; Edlinger, C.; Sieber, S.; Goers, R.; Najer, A.; Spulber, M.; Onaca-Fischer, O.; Huwyler, J.; Palivan, C. G. Biomimetic Artificial Organelles with in Vitro and in Vivo Activity Triggered by Reduction in Microenvironment. *Nat. Commun.* **2018**, *9*, 1127.

(18) Liu, S.; Zhang, Y.; Li, M.; Xiong, L.; Zhang, Z.; Yang, X.; He, X.; Wang, K.; Liu, J.; Mann, S. Enzyme-Mediated Nitric Oxide Production in Vasoactive Erythrocyte Membrane-Enclosed Coacervate Crotocells. *Nat. Chem.* **2020**, *12*, 1165−1173.

(19) Chen, Y.; Tan, J.; Zhang, Q.; Xin, T.; Yu, Y.; Nie, Y.; Zhang, S. Artificial Organelles Based on Cross-Linked Zwitterionic Vesicles. *Nano Lett.* **2020**, *20*, 6548−6555.

(20) Xi, J.; Zhang, R.; Wang, L.; Xu, W.; Liang, Q.; Li, J.; Jiang, J.; Yang, Y.; Yan, X.; Fan, K.; Gao, L. A Nanozyme-Based Artificial Peroxisome Ameliorates Hyperuricemia and Ischemic Stroke. *Adv. Funct. Mater.* **2021**, *31*, 2007130.

(21) Rideau, E.; Dimova, R.; Schwille, P.; Wurm, F. R.; Landfester, K. Liposomes and Polymersomes: a Comparative Review towards Cell Mimicking. *Chem. Soc. Rev.* **2018**, *47*, 8572−8610.
(22) Matoori, S.; Leroux, J.-C. Twenty-five Years of Polymersomes: Lost in Translation? *Mater. Horiz.* **2020**, *7*, 1297−1309.
(23) Miller, A. J.; Pearce, A. K.; Foster, J. C.; O'Reilly, R. K. Probing and Tuning the Permeability of Polymersomes. *ACS Cent. Sci.* **2021**, *7*, 30−38.
(24) Crommelin, D. J. A.; van Hoogevest, P.; Storm, G. The Role of Liposomes in Clinical Nanomedicine Development. What now? Now what? *J. Controlled Release* **2020**, *318*, 256−263.
(25) Le Meins, J. F.; Schatz, C.; Lecommandoux, S.; Sandre, O. Hybrid Polymer/Lipid Vesicles: State of the Art and Future Perspectives. *Mater. Today* **2013**, *16*, 397−402.
(26) Schulz, M.; Binder, W. H. Mixed Hybrid Lipid/Polymer Vesicles as a Novel Membrane Platform. *Macromol. Rapid Commun.* **2015**, *36*, 2031−2041.
(27) Liu, D.; Sun, H.; Xiao, Y.; Chen, S.; Cornel, E. J.; Zhu, Y.; Du, J. Design Principles, Synthesis and Biomedical Applications of Polymer Vesicles with Inhomogeneous Membranes. *J. Controlled Release* **2020**, *326*, 365−386.
(28) Meyer, C. E.; Abram, S.-L.; Craciun, I.; Palivan, C. G. Biomolecule−Polymer Hybrid Compartments: Combining the Best of Both Worlds. *Phys. Chem. Chem. Phys.* **2020**, *22*, 11197−11218.
(29) Dao, T. P. T.; Fernandes, F.; Fauquignon, M.; Ibarboure, E.; Prieto, M.; Le Meins, J. F. The Combination of Block Copolymers and Phospholipids to Form Giant Hybrid Unilamellar Vesicles (GHUVs) Does not Systematically Lead to "Intermediate" Membrane properties. *Soft Matter* **2018**, *14*, 6476−6484.
(30) Otrin, L.; Marusic, N.; Bednarz, C.; Vidakovic-Koch, T.; Lieberwirth, I.; Landfester, K.; Sundmacher, K. Toward Artificial Mitochondrion: Mimicking Oxidative Phosphorylation in Polymer and Hybrid Membranes. *Nano Lett.* **2017**, *17*, 6816−6821.
(31) Passos Gibson, V.; Fauquignon, M.; Ibarboure, E.; Leblond Chain, J.; Le Meins, J.-F. Switchable Lipid Provides pH-Sensitive Properties to Lipid and Hybrid Polymer/Lipid Membranes. *Polymers-Basel* **2020**, *12*, 637.
(32) Paxton, W. F.; McAninch, P. T.; Achyuthan, K. E.; Shin, S. H. R.; Monteith, H. L. Monitoring and Modulating Ion Traffic in Hybrid Lipid/Polymer Vesicles. *Colloids Surf. B Biointerfaces* **2017**, *159*, 268−276.
(33) Mumtaz Virk, M.; Reimhult, E. Phospholipase A2-Induced Degradation and Release from Lipid-Containing Polymersomes. *Langmuir* **2018**, *34*, 395−405.
(34) Zong, W.; Thingholm, B.; Itel, F.; Schattling, P. S.; Brodszkij, E.; Mayer, D.; Stenger, S.; Goldie, K. N.; Han, X.; Städler, B. Phospholipid−Block Copolymer Hybrid Vesicles with Lysosomal Escape Ability. *Langmuir* **2018**, *34*, 6874−6886.
(35) Brodszkij, E.; Hviid, M. J.; Ade, C.; Schattling, P. S.; Burmeister, M.; Szilagyi, S.; Gal, N.; Zhu, C.; Han, X.; Städler, B. Interaction of pH-responsive polyanions with phospholipid membranes. *Polym. Chem.* **2019**, *10*, 5992−5997.
(36) Brodszkij, E.; Westensee, I. N.; Bertelsen, M.; Gal, N.; Boesen, T.; Städler, B. Polymer−Lipid Hybrid Vesicles and Their Interaction with HepG2 Cells. *Small* **2020**, *16*, 1906493.
(37) Ukawa, M.; Akita, H.; Masuda, T.; Hayashi, Y.; Konno, T.; Ishihara, K.; Harashima, H. 2-Methacryloyloxyethyl phosphorylcholine polymer (MPC)-Coating Improves the Transfection Activity of GALA-Modified Lipid Nanoparticles by Assisting the Cellular Uptake and Intracellular Dissociation of Plasmid DNA in Primary Hepatocytes. *Biomaterials* **2010**, *31*, 6355−62.
(38) Komin, A.; Russell, L. M.; Hristova, K. A.; Searson, P. C. Peptide-based Strategies for Enhanced Cell Uptake, Transcellular Transport, and Circulation: Mechanisms and Challenges. *Adv. Drug Delivery Rev.* **2017**, *110*−*111*, 52−64.
(39) Zelmer, C.; Zweifel, L. P.; Kapinos, L. E.; Craciun, I.; Güven, Z. P.; Palivan, C. G.; Lim, R. Y. H. Organelle-specific Targeting of Polymersomes into the Cell Nucleus. *Proc. Natl. Acad. Sci. U.S.A* **2020**, *117*, 2770−2778.
(40) De Dios Andres, P.; Westensee, I. N.; Brodszkij, E.; Ramos-Docampo, M. A.; Gal, N.; Stadler, B. Evaluation of Hybrid Vesicles in an Intestinal Cell Model Based on Structured Paper Chips. *Biomacromolecules* **2021**, *22*, 3860−3872.
(41) Taipaleenmaki, E.; Brodszkij, E.; Stadler, B. Mucopenetrating Zwitterionic Micelles. *Chemnanomat* **2020**, *6*, 744−750.
(42) Nakase, I.; Futaki, S. Combined Treatment with a pH-Sensitive Fusogenic Peptide and Cationic Lipids Achieves Enhanced Cytosolic Delivery of Exosomes. *Sci. Rep.* **2015**, *5*, 10112.
(43) Schach, D. K.; Rock, W.; Franz, J.; Bonn, M.; Parekh, S. H.; Weidner, T. Reversible Activation of a Cell-Penetrating Peptide in a Membrane Environment. *J. Am. Chem. Soc.* **2015**, *137*, 12199−12202.
(44) Palominos, M. A.; Vilches, D.; Bossel, E.; Soto-Arriaza, M. A. Interaction between Amphipathic Triblock Copolymers and L-alpha-dipalmitoyl phosphatidylcholine Large Unilamellar Vesicles. *Colloids Surf. B Biointerfaces* **2016**, *148*, 30−40.
(45) Hou, X.; Zaks, T.; Langer, R.; Dong, Y. Lipid Nanoparticles for mRNA Delivery. *Nat. Rev. Mater.* **2021**, *6*, 1078−1094.
(46) Ermilova, I.; Swenson, J. DOPC versus DOPE as a Helper Lipid for Gene-therapies: Molecular Dynamics Simulations with DLin-MC3-DMA. *Phys. Chem. Chem. Phys.* **2020**, *22*, 28256−28268.
(47) Litzinger, D. C.; Huang, L. Phosphatidylethanolamine Liposomes: Drug Delivery, Gene Transfer and Immunodiagnostic Applications. *Biochim. Biophys. Acta* **1992**, *1113*, 201−27.
(48) Wang, J.; Ayano, E.; Maitani, Y.; Kanazawa, H. Tunable Surface Properties of Temperature-Responsive Polymer-Modified Liposomes Induce Faster Cellular Uptake. *ACS Omega* **2017**, *2*, 316−325.
(49) Dunn, K. W.; Kamocka, M. M.; McDonald, J. H. A Practical Guide to Evaluating Colocalization in Biological Microscopy. *Am. J. Physiol. Cell Physiol.* **2011**, *300*, C723−42.
(50) Montizaan, D.; Yang, K.; Reker-Smit, C.; Salvati, A. Comparison of the Uptake Mechanisms of Zwitterionic and Negatively Charged Liposomes by HeLa Cells. *Nanomedicine* **2020**, *30*, 102300.

https://doi.org/10.1021/acs.biomac.1c01403
Biomacromolecules 2022, 23, 1052−1064